

The anti-distortive polaron as an alternative mechanism for lattice-mediated charge trapping

Received: 5 April 2024

Accepted: 29 January 2025

Published online: 16 February 2025

 Check for updates

Hamideh Hassani^{1,2}, Eric Bousquet ¹, Xu He¹, Bart Partoens² & Philippe Ghosez ¹ 

Polarons can naturally form in materials from the interaction of extra charge carriers with the atomic lattice. Ubiquitous, they are central to various phenomena such as high- T_c superconductivity, electrochromism, photovoltaics, photocatalysis or ion batteries. However, polaron formation remains poorly understood and mostly relies on historical models such as Landau–Pekar, Fröhlich, Holstein or Jahn–Teller polarons. Here, from advanced first-principles calculations, we show that the formation of intriguing medium-sized polarons in WO_3 does not fit with traditional models but instead arises from the local undoing of distortive atomic motions inherent to the pristine phase, which lowers the bandgap through dynamical covalency effects and drives charge trapping. We introduce the concept of the anti-distortive polaron and rationalize it from a quantum-dot model. We demonstrate that anti-distortive polarons are generic to different families of compounds and clarify how this new concept opens concrete perspectives for a better control of the polaronic state and related properties.

Polarons consist in the spatial localization of excess charge carriers in crystals, through their interaction with the surrounding atomic lattice and the subsequent deformation of the latter¹. As such, polarons can be seen as quasiparticles consisting of an electron or a hole, dressed by a cloud of virtual phonons attached to and moving with it. Depending on the crystal and strength of the electron-phonon interaction, polarons can be large or small but will inevitably affect electronic properties, making the concept of polaron a central, timely, and ubiquitous topic in material science². As such, it is nowadays at the heart of active research in photovoltaics³, photocatalysis⁴, electrochromism⁵ or ion batteries⁶.

Anticipated by Landau⁷, the concept of polaron was first coined by Pekar⁸, from a model describing the interaction of an electron with a continuous polarizable medium. Following the same line of thought, Fröhlich^{9,10} then provided a more rigorous quantum mechanical description, relying on long-range Coulombic electron-phonon interactions. The addition of an extra charge in a polar

crystal lattice naturally induces dielectric screening from the activation of longitudinal optical polar phonons, yielding the formation of a polaron, the spatial extension of which depends on the dielectric constant of the medium. This typically applies to large polarons extending over multiple sites in ionic and polar crystals. Independently, Holstein^{11,12} provided an alternative and more atomistic description, relying on short-range electron-phonon interactions involving acoustic phonons. Local elastic deformations can create a small quantum dot trapping the charge and can explain the formation of small polarons, usually confining the charge on one single site. Later, the concept of Jahn–Teller polaron was also introduced by Hock, Nickisch, and Thomas¹³ and appeared as an alternative mechanism for small polaron formation in a system with Jahn–Teller active ions. In the presence of degenerated energy levels, the addition of an extra charge can activate a local Jahn–Teller distortion that splits the energy levels and stabilizes the charge on a given site. Such a concept of Jahn–Teller polaron is intimately linked to important

¹Theoretical Materials Physics, Q-MAT, University of Liège, Liège, Belgium. ²Department of Physics, University of Antwerp, Antwerp, Belgium.

 e-mail: Philippe.Ghosez@uliege.be

phenomena such as colossal magnetoresistance in manganites^{14,15} or the high- T_c superconductivity in cuprates¹⁶. All these consecutive models are still the backbone of present polaron interpretations. They remain however more conceptual than real tools for quantitative predictions.

Polarons are nowadays also accessible to density functional theory (DFT) calculations, although their first-principles study remains challenging¹⁷. A first limitation in direct calculations is the size of simulation boxes, restricting practical investigations to small polarons^{18,19}. This drawback has been recently overcome with the development of an elegant formalism requiring only the computation of quantities within the primitive cell²⁰. Including all kinds of electron-phonon interactions, this approach provides moreover a unified formalism for addressing large and small polarons. A second difficulty is to properly reproduce charge localization using usual local exchange-correlation functionals, that include spurious self-interactions. However, more advanced self-interaction corrections^{21,22}, DFT+U^{23,24}, and hybrid functionals^{24,25} often reproduce polarons in fair agreement with experimental data. Thanks to this recent progress, there has been a renewed interest in polarons¹⁷, with the hope that DFT could unravel meaningful new insights in polaron formation and important related phenomena.

WO₃ is often considered as a paradigmatic polaronic compound^{26,27}. Although the unusual medium size and disk-like shape of its polarons were already revealed in the experimental work of Salje²⁷, the origin of such polarons remains unclear. Here, relying on first-principles investigations, we show that classical polaron models do not strictly apply to WO₃. Instead, we introduce the concept of anti-distortive polaron, in which charge localization arises from the undoing of some inherent distortive motions. We rationalize our findings with a simple generic model and further demonstrate the generality of the concept and its concrete practical implications.

Results

Structurally, WO₃ can be seen as an ABO₃ perovskite with missing A cation: its $Pm\bar{3}m$ cubic reference structure consists in a network of corner-shared oxygen octahedra, with W atoms at their centers²⁸. On cooling, it exhibits a complex sequence of structural phase transitions toward a monoclinic ground state, originally considered as of Pc symmetry^{26,29} but better assigned now as $P2_1/c$ ^{30,31}. Electronically, it is a wide bandgap semiconductor³². In practice however, it is typically sub-stoichiometric (WO_{3- δ}), which makes it intrinsically n -doped. Then, those extra electrons are known to form polarons and even bi-polarons, which are expected to be closely associated with the remarkable electrical, chromic and superconducting properties of WO₃^{5,33-35}.

Accurate simulation of a self-trapped single polaron in WO₃ from DFT has only been reported recently^{25,36,37}. Those calculations properly captured the spatial extension of the polaron over a few unit cells, together with its unusual disk-like shape. Building on those seminal results, we start here with a careful analysis of the polaron structural distortion in order to unravel the microscopic mechanism behind its formation.

Our investigations are performed in the framework of DFT using a full hybrid-functional approach on large supercells (up to 576 atoms), which was previously shown to provide an accurate description of polarons in WO₃²⁵. To study polaron formation, an extra electron is added to the system while charge neutrality is restored by the inclusion of a positive background (see method section). The atomic distortion is then analyzed from its projection on phonon eigendisplacements of the reference ($Pm\bar{3}m$) and ground-state ($P2_1/c$) phases.

The reference $Pm\bar{3}m$ cubic phase of WO₃ shows various phonon instabilities^{30,31}, in line with its complex sequence of structural phase transitions with temperature. The largest instability is a polar mode (Γ_4^-) at the Brillouin-zone center that could make WO₃ ferroelectric. However, the ground state and room temperature phases are both non-polar and show instead $P2_1/c$ and $P2_1/n$ symmetries³⁰. These

phases can be described as small distortions $|\Delta\rangle$ with respect to the cubic phase, that arises from the condensation of distinct unstable modes $|\eta_i^c\rangle$ of this cubic phase (i.e., $|\Delta\rangle = \sum_i Q_i |\eta_i^c\rangle$). In the ground-state $P2_1/c$ phase³⁰, the distortion $|\Delta_{GS}\rangle$ is dominated by the condensation of (i) unstable antipolar motions of W against O atoms along the z axis, $|\eta_M^c\rangle$ (M_3^- mode lowering the symmetry from $Pm\bar{3}m$ to $P4nm$), and (ii) additional unstable antiphase rotations of the O octahedra, $|\eta_R^c\rangle$ (R_4^+ mode), that further produce together the appearance of (iii) secondary antipolar motions in the xy plane, $|\eta_X^c\rangle$ (X_5^- mode), through improper coupling³⁰. In the room temperature $P2_1/n$ phase³⁰, the distortion $|\Delta_{RT}\rangle$ involves similar modes, but differently oriented, and also includes additional in-phase oxygen rotations (M_3^+ mode), which importantly reduce the X_5^- in-plane antipolar motions along x direction. Our approach nicely reproduces the geometry of both phases (see ref. 31 using the same method) and describes the $P2_1/c$ ground state as an insulator with a bandgap of 3.4 eV, in close agreement with the experimental value ($E_g \approx 3.25\text{--}3.4$ eV^{32,38}).

Adding an extra electron to the system, it should a priori occupy a state at the bottom of the conduction band, delocalized over the whole crystal (the left panel of Fig. 1a, b). However, and consistent with previous calculations²⁵, the proper coupling of this original state with atomic relaxations leads to the formation of a polaron level below the conduction band edge, with the charge located mainly on a central W atom and spreading partly over the first and second W neighbors (the right panel of Fig. 1a, d). In line with experimental expectations by Salje²⁷ (Fig. 1f), the polaron charge is confined in a single xy plane (Fig. 1g) showing a strongly anisotropic and characteristic 2D disk-like shape (radius $R_p \approx 7.5\text{--}8.5$ Å). This unusual shape originates from the fact that, in the $P2_1/c$ phase, the lowest conduction level giving rise to the polaron state is made of strongly directional d_{xy} orbitals. Distinctly from the original report²⁵, our more converged calculations in a bigger supercell locates the polaron state 520 meV below the delocalized state (see also Supplementary Note 1), supporting the spontaneous formation of polarons at low temperature in the $P2_1/c$ phase of WO₃.

While the polaron charge is rather isotropically distributed in the xy plane (flat disk-like shape, Fig. 1d), the related atomic distortion $|\Delta_{pol}\rangle$, illustrated in Fig. 1c, is intriguingly asymmetric. In order to clarify the nature of $|\Delta_{pol}\rangle$, we can project it on the phonon modes $|\eta_i^m\rangle$ of the monoclinic $P2_1/c$ phase. The dominant contributions are highlighted in Figs. 2d, e and are distributed all over the Brillouin zone. Amazingly, focusing first on the Brillouin-zone center (Γ point), we do not see any significant involvement of polar, Jahn–Teller, or acoustic modes as expected from usual Fröhlich, Jahn–Teller or Holstein models (see also Supplementary Note 2, Supplementary Table II). Instead, the major contribution at Γ comes intriguingly from non-polar Raman modes $|\eta_{Ra}^m\rangle$. They are these modes that are mainly responsible for the atomic distortion pattern in the polaron core region, but which alone would reproduce this Raman distortion homogeneously to the whole crystal (see Supplementary Note 2, Supplementary Fig. 3). Then, additional non- Γ phonon modes are also activated: those yield a global distortion that cancels out the Raman-type distortion outside the core region (see Supplementary Note 2, Supplementary Fig. 3) and are so responsible for the local character of $|\Delta_{pol}\rangle$. As a whole, $|\Delta_{pol}\rangle$ can therefore be seen as a zone-center Raman-type distortion produced by $|\eta_{Ra}^m\rangle$, but localized over only a few unit cells around the polaron core.

At a more atomistic level, the W environment is asymmetric in the pristine $P2_1/c$ phase and, in practice, the polaron distortion acts in order to make this environment more symmetric (Fig. 1e). Projection of $|\eta_{Ra}^m\rangle$ on the phonons of the cubic phase identifies it as a linear combination of $|\eta_R^c\rangle$ and $|\eta_X^c\rangle$ inherent to the $P2_1/c$ phase distortion $|\Delta_{GS}\rangle$ but oriented in order to cancel it (see Supplementary Note 2, Supplementary Table III). As such, the polaron formation here should not be seen as the activation of an additional virtual phonon cloud attempting to screen the extra charge as in traditional models but, instead, as the local undoing of the $|\eta_R^c\rangle$ and $|\eta_X^c\rangle$ distortive motions,

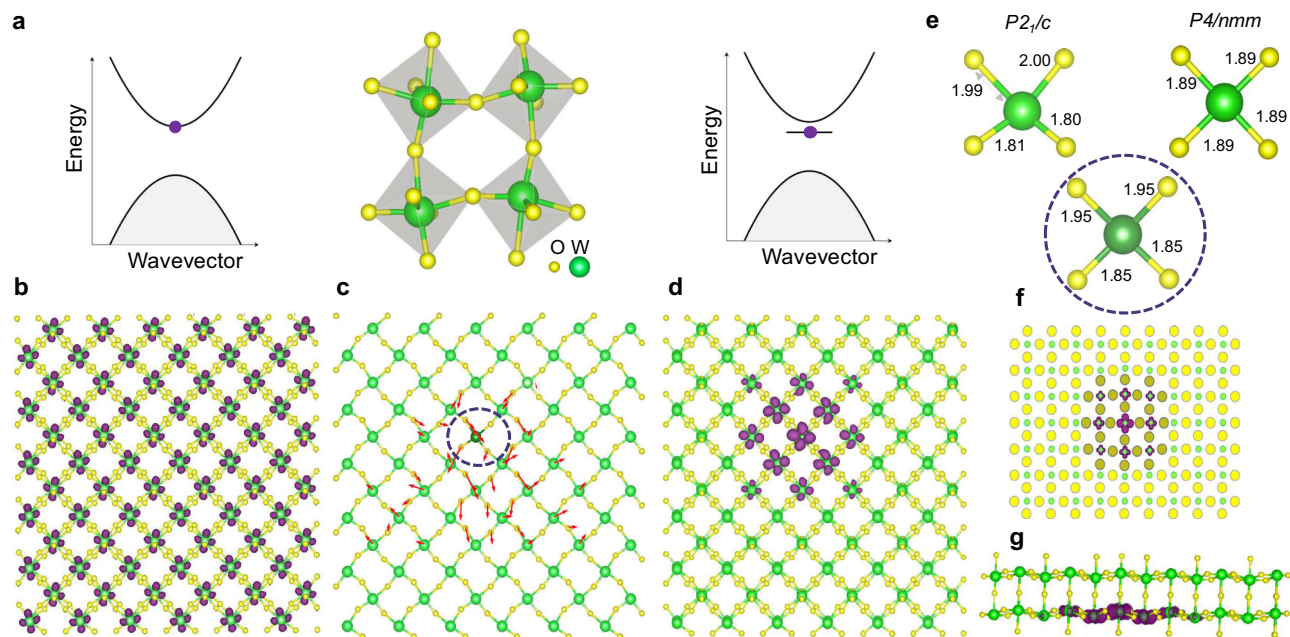


Fig. 1 | Polaron in the $P2_1/c$ phase of WO_3 (W atoms in green and O atoms in yellow). **a** Sketch of the atomic structure (center) and of the electronic bands, when adding an extra electron, in the free carrier (left) and polaron (right) cases. **b** Computed charge density map (in purple) of a fully delocalized extra electron in the xy plane of the $P2_1/c$ phase. **c** Computed atomic distortion (red arrows) associated to the formation of a single polaron in the $P2_1/c$ phase. **d** Computed charge density map

(in purple) of a single polaron in the xy plane of the $P2_1/c$ phase. **e** Comparison of the atomic environment of the polaron central W atom (within the dashed-line circle area in **c**) with that in the pristine $P2_1/c$ and $P4/nmm$ phases (interatomic distances in Å). **f** Experimental charge density map of a single polaron in the $P2_1/c$ phase as reported by Salje (based on ref. 27). **g** Side view of the computed charge density (in purple) of a single polaron in the $P2_1/c$ phase, highlighting its 2-dimensional character.

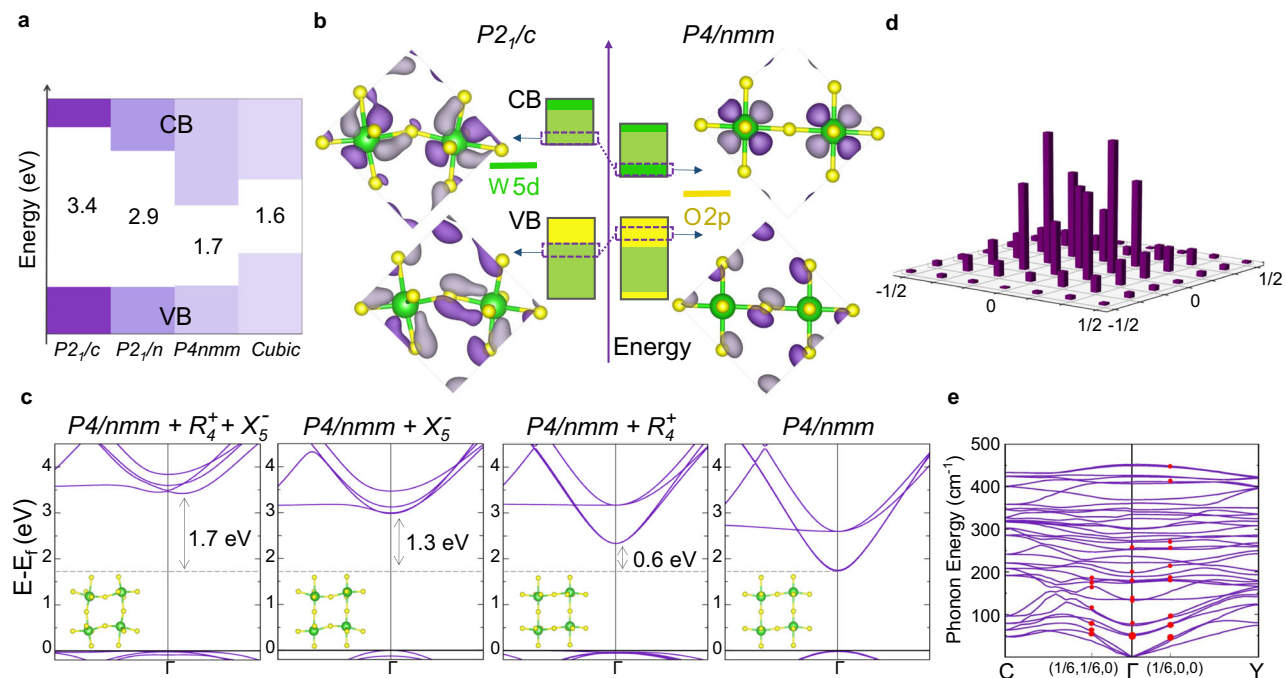


Fig. 2 | Electronic and phonon properties of WO_3 (W atoms in green and O atoms in yellow). **a** Comparison of the electronic bandgap amplitudes (in eV) and position of the valence band (VB) and conduction band (CB) edges in distinct phases of WO_3 . **b** Simple sketch of the valence and conduction bands in the $P2_1/c$ (left) and $P4/nmm$ (right) phases of WO_3 , with yellow and green area highlighting respectively the positions of O $2p$ and W $5d$ states. The change of hybridization between O $2p$ and W $5d_{xy}$ orbitals, yielding the gap opening under atomic distortions from $P4/nmm$ to $P2_1/c$, are illustrated from the evolution of wavefunctions

valence and conduction states at Γ . **c** Evolution of the electronic band structure of the $P4/nmm$ phase of WO_3 when condensing the X_5^- in-plane antipolar motion, and R_4^+ oxygen rotation motions, bringing the system toward the $P2_1/c$ phase. **d** Contributions to the polaron atomic distortion of phonon modes at distinct $(q_x, q_y, 0)$ points of first Brillouin zone of the $P2_1/c$ phase (using a $6 \times 6 \times 1$ supercell). **e** Contributions to the polaron atomic distortion of distinct phonon modes from Γ and $\Gamma - C$ and $\Gamma - Y$ lines of first Brillouin zone of the $P2_1/c$ phase. Amplitudes of respective contributions are proportional to the red circles' radii.

originally present in the pristine $P2_1/c$ phase, in order to drive the system closer to the more symmetric $P4/nmm$ phase ($Q_R = Q_X = 0$). As such, and in analogy with anti-Jahn–Teller polarons³⁹, we coin here the name of anti-distortive polaron.

Looking at the various metastable phases of WO_3 ³⁰, it appears in Fig. 2a that the electronic bandgap is much larger in the $P2_1/c$ (3.4 eV) and $P2_1/n$ (2.9 eV) phases than in the $P4/nmm$ phase (1.7 eV), which is in line with previous theoretical and experimental reports^{30,40} and can be rationalized as follows (see also Supplementary Note 3, Supplementary Fig. 4). The bandgap in WO_3 is typically between valence and conduction states respectively of dominant O $2p$ and W $5d t_{2g}$ character⁴¹. In the reference cubic phase, all three t_{2g} states are degenerated at the bottom of the conduction band. In the $P4/nmm$ phase in which all in-plane W–O bonds are equivalent, the condensation of M_3^- antipolar motions along z has pushed up d_{xz} and d_{yz} states so that the lowest conduction states are of d_{xy} character. Then, the appearance of X_5^- antipolar in-plane motion, and to a lower extent R_4^+ oxygen rotation motions, create alternating short and long W–O bonds in-plane. This amplifies hybridizations between the occupied O $2p$ and empty W $5d_{xy}$ states and significantly opens the bandgap by lowering, in the valence band, the occupied state localizing the charge in the short W–O bond and by moving up, in the conduction band, the empty state localizing the charge in the long W–O bond (Fig. 2b, c). Our conjecture is therefore that, in order to form the polaron, the system suppresses locally the X_5^- and R_4^+ atomic distortions inherent to the pristine $P2_1/c$ phase in order to lower the conduction state there and trap the extra charge at a lower energy. This mechanism is reminiscent of the phase transformations previously reported in WO_3 over heavy doping⁴².

As a first proof of concept, we built a supercell of the $P2_1/c$ phase, in which we artificially imposed $Q_R = Q_X = 0$ around the central unit cell (see Supplementary Note 4, Supplementary Fig. 9a) to bring the system back there to $P4/nmm$. Adding an extra electron to that frozen structure, it naturally localizes in the central region, showing features similar to the relaxed polaron (see Supplementary Note 4, Supplementary Fig. 9b). This confirms the possibility to achieve charge localization from the tuning of Raman mode distortions but it does not demonstrate that such a mechanism will spontaneously appear.

In order to go one step further, we developed a simple quantum-dot model⁴³ (see Supplementary Note 5). Adding an extra electron to the system, it should a priori occupy the lowest conduction energy level and delocalize over the whole crystal (Fig. 1b), which defines our reference energy state. Starting from there, forming a polaron requires activating the atomic distortion $|\Delta_{pol}|$ in the dynamically stable $P2_1/c$ phase. This costs an energy $E_{latt}(x, R)$ which scales both with the amplitude x of the Raman-type atomic distortion $|\eta_{Ra}^m\rangle$ associated to the polaron (with x normalized to 1 in the polaron structure relaxed in DFT) and the radius R of the region within which this distortion appears. Concomitantly, condensing a Raman distortion $|\eta_{Ra}^m\rangle$ of amplitude x in the $P2_1/c$ phase lowers the lowest conduction state containing the extra electron, producing then a lowering of electronic energy $E_{elec}(x)$. The latter is an electronic band term, expected when condensing $|\eta_{Ra}^m\rangle$ homogeneously over the whole crystal. Restricting the distortion over a spatial region of radius R will further localize the extra electron in this region and so produce an extra energy cost $E_{conf}(x, R)$ due to the confinement of the electron. In this context, the polaron formation energy can be written as

$$E_f^{pol} = \min_{(x, R)} \{ E_{latt}(x, R) + E_{elec}(x) + E_{conf}(x, R) \} \quad (1)$$

and the polaron will form spontaneously as soon as the lowering of E_{elec} produced by the appearance of the Raman distortion compensates the energy costs produced by E_{latt} and E_{conf} .

The explicit (x, R) dependence and parameters of all three energy terms can be independently estimated from DFT calculations

(see Supplementary Note 5, Supplementary Equation 6). Then, determining E_f^{pol} from the minimization in Eq. (1) will not only tell us if the polaron will naturally appear (i.e., $E_f^{pol} < 0$) but also what is the spatial extension R and distortion amplitude x at the minimum. As discussed in Supplementary Note 5, the model calculations reproduce the formation of a polaron over a relatively broad range of effective masses entering into $E_{conf}(x, R)$. Moreover, a formation energy ($E_f^{pol} \approx -100$ meV), polaron radius ($R_p \approx 8$ Å) and distortion amplitude ($x \approx 1$) comparable to DFT data are obtained consistently for realistic values of the parameters.

The ability of this simple quantum dot model to reproduce, with realistic parameters, the results achieved from the fully self-consistent DFT atomic relaxation, provides strong support to our initial conjecture that polaron formation in the $P2_1/c$ phase of WO_3 arises from local lowering of the bandgap achieved from the partial undoing of the atomic distortions inherent to the pristine phase. According to this picture, the distinct phases of WO_3 should not be similarly prone to form polarons. Consistently with that, in the room-temperature $P2_1/n$ phase, which shows smaller Q_X along x and a lower bandgap, polarons become much more delocalized in our calculations (see Supplementary Note 6, Supplementary Fig. 12), as also confirmed experimentally²⁷. Then, in the $P4/nmm$ phase ($Q_R = Q_X = 0$), we were unable to stabilize any similar polaronic state.

Discussion

The above results highlight the natural formation of stable polarons in WO_3 , arising from the local undoing of non-polar distortive motions (inherent to the pristine phase), which tunes orbital hybridizations, locally lowers the conduction state and drives the charge localization. This was not anticipated in previous studies^{25,36,37,44} and we coin the name of anti-distortive polaron for this alternative mechanism of lattice-mediated charge trapping.

It is worth contrasting this anti-distortive polaron with traditional conceptual models that were better expected to apply to WO_3 . In WO_3 , the strong polar character of the compound (giant Born effective charges Z^{*45} , soft polar mode in the cubic phase) was naturally pointing in the direction of an efficient dielectric screening of the extra charge through the activation of longitudinal optical polar modes in line with Landau–Pekar–Fröhlich models or of a ferroelectric polaron. However, our DFT calculations show that no significant polar motion is involved in the polaron distortion. Alternatively, WO_3 might also be prone to form Jahn–Teller polarons due to the Jahn–Teller active character of the W ion. However, the polaron distortion in the $P2_1/c$ phase does not overlap with Jahn–Teller motions either. The present anti-distortive polaron of WO_3 shows closer similarities with small Holstein polarons in the sense that charge trapping relates to the formation of a quantum dot. However, while the conventional Holstein polaron is typically linked to the activation of a local elastic response induced by the extra charge, here the mechanism involves changes of hybridizations driven by the undoing of soft atomic motions inherent to the displacive nature of the compound. The unusual medium size of the polaron in WO_3 supports that both mechanisms are not necessarily strictly equivalent.

The case of WO_3 could be a bit specific since the absence of the A cation gives rise to large distortions and the $5d$ character of W makes the d states particularly delocalized, but the mechanism of anti-distortive polaron is a priori totally generic and should more broadly apply to various displacive compounds like some related ABO_3 perovskites. The latter are typically mixed ionic-covalent compounds and their giant Z^* testify of the strong sensitivity of orbital hybridization to atomic displacements⁴⁶. Depending on their Goldschmidt tolerance factor⁴⁷, ABO_3 compounds are prone to develop different kinds of structural distortions⁴⁸, which are known to tune their bandgap, and could get similarly involved in polaron formation.

As a guiding rule, inspection of the electronic bandgap and its evolution from phase to phase might be a good indicator to track the

eventual propensity of alternative compounds to develop analogous anti-distortive polarons. A quick search in materials databases for compounds showing large increase of bandgap from a high-symmetry to a lower-symmetry phase, provides a long list of perovskite and even non-perovskite potential candidates, including WO_3 (see Supplementary Note 7). All of them might not be relevant since other aspects need to be considered, such as the nature of the bandgap. Nevertheless, considering for instance $P2_1/c$ MoO_3 (isostructural to WO_3) or $Pnma$ YAlO_3 and $P2/c$ YTaO_4 as representative members of the perovskite $R(\text{Al}/\text{Ga})\text{O}_3$ and fergusonite $R(\text{Ta}/\text{Nb})\text{O}_4$ families of compounds (with $R = \text{Y}$ or a rare-earth) and adding an extra electron, we can stabilize in those compounds an anti-distortive electronic polaron (see Supplementary Note 7, and Supplementary Figs. 13, 15, 16) arising from the partial undoing of distortive motions, exactly as in WO_3 . This illustrates concretely the generality of the reported mechanism that might also be relevant to many other families of displacive compounds.

While anti-distortive polarons emerge from the undoing of distortive motions that had opened the electronic bandgap in the pristine phase, we could imagine alternatively distortive polarons activating instead a distortion lowering the conduction states. This points out some interesting connections with (anti)Jahn–Teller polarons^{16,39,49}. But while in Jahn–Teller polarons the tuning of the gap arises from on-site splitting of degenerated states from the Jahn–Teller effect, in anti-distortive polarons, it is linked to inter-site covalency effects and the tuning of bonding-antibonding states. It is worth noticing that the present discussion also links to the metal-insulator transition in rare-earth nickelates in which the activation of distortive breathing oxygen motions lower energy states to localize the charge at some sites and is sometimes interpreted as a polaron condensation⁵⁰.

In conclusion, the present concept of anti-distortive polaron is not only of academic interest. Appearing relevant to various compounds, it naturally connects to various fields including electrochromism⁵, high- T_c superconductivity^{16,35}, colossal magneto-resistance^{14,15,35}, photovoltaics³, photocatalysis⁴ or ion batteries⁶. Moreover, the distinct behaviors highlighted in the $P2_1/c$, $P2_1/n$ and $P4/nmm$ phases of WO_3 (see Supplementary Note 6) demonstrate explicitly the strong sensitivity of the polaronic state with the amplitude of distortive motions. In WO_3 ⁵¹, related perovskites⁴⁸ and other displacive compounds, phase stability and distortive motions can nowadays be efficiently monitored by strain⁵² and interface^{53,54} engineerings, electric fields⁵⁵ or optical pulses⁵⁶. So, linking explicitly here polarons in some compounds to tunable distortive motions, we open de facto concrete perspectives to achieve in those compounds rational static or dynamical control of the polaronic state and of its related properties by external fields.

Methods

Calculations were performed in the framework of DFT, using the B1-WC hybrid functional⁵⁷ – updated with 20% of exact exchange – as implemented in the CRYSTAL17 code⁵⁸. We use all-electron double- ζ basis sets for oxygen whereas, for the heavy tungsten atom, we use the effective core pseudopotential (ECP) technique – as implemented in the small core Detlev-Figgen pseudopotentials – associated with the correlation-consistent polarized valence triple- ζ basis set (cc-pVDZ)⁵⁹ for the explicit treatment of valence electrons.

We have simulated the polaron by adding an extra electron into the system, with charge neutrality being ensured by a compensating positively charged background. Such a free-carrier charge trapping method^{25,44} avoid the complexities of considering the presence of donor cations and structural disorders, enabling us to solely investigate the effects of the extra charge rather than other factors. The use of this method is also justified by the experimental observation that self-trapped electrons in WO_3 are disconnected from their defect origin²⁷.

Calculations were carried out on distinct supercells to check convergency of the results. The reported results correspond to a supercell including 576 atoms and consisting in a $6 \times 6 \times 1$ repetition of

the $P2_1/c$ unit cell (one $P2_1/c$ unit cell contains sixteen atoms: four W and twelve O). Integrations over the Brillouin zone have been performed on a $1 \times 1 \times 4$ grid of k-points for the $6 \times 6 \times 1$ supercell.

Structural atomic relaxations of the doped system were carried using lattice parameters fixed to those of the pristine $P2_1/c$ ground-state phase. The relaxation was stopped when the root mean square of the gradient and displacements were smaller than 5×10^{-5} Ha/Bohr and 10^{-3} Bohr, respectively.

The calculations were spin-polarized and the overall magnetic moment was constrained to be $1 \mu_B$ during the first steps of the calculations, to stabilize the ferromagnetic (FM) solution and the polaron formation.

AGATE software⁶⁰ was used to project the atomic distortions onto the phonon modes of the cubic and monoclinic phases (mode-by-mode decomposition analysis).

The above computational approach was checked to provide results equivalent to what was previously reported in ref. 31, demonstrating an excellent description of the structural, electronic, and phonon properties of the different phases of WO_3 . The present results show some similarities with the polaronic state previously reported in ref. 25 but the present calculations are better converged, highlighting then some key differences and yielding distinct analysis and interpretation, as pointed out in the main text.

Data availability

Relevant data supporting the different claims are provided in the Supplementary Information file, which includes seven notes. If needed, extra data are available from the corresponding author upon request.

Code availability

The data presented in this study were generated using broadly accessible first-principles packages, as described in the Methods section.

References

- Emin, D. *Polarons* (Cambridge University Press, 2012). <https://doi.org/10.1017/CBO9781139023436>.
- Alexandrov, A. & Devreese, J.T. *Advances in Polaron Physics* (Springer-Verlag, 2010). <https://doi.org/10.1007/978-3-642-01896-1>.
- Zhang, H. & Park, N. G. Polarons in perovskite solar cells: effects on photovoltaic performance and stability. *J. Phys. Energy* **5**, 024002 (2023).
- Ren, Z., Shi, Z., Feng, H., Xu, Z., Hao, W. Recent progresses of polarons: Fundamentals and roles in photocatalysis and photoelectrocatalysis. *Adva. Sci.* **n/a**, 2305139. <https://doi.org/10.1002/adv.202305139>.
- Deb, S. K. Opportunities and challenges in science and technology of WO_3 for electrochromic and related applications. *Sol. Energy Mater. Sol. Cells* **92**, 245–258 (2008).
- Luong, H. D., Tran, T. L., Phung, V. B. T. & Dinh, V. A. Small polaron transport in cathode materials of rechargeable ion batteries. *J. Sci. Adv. Mater. Devices* **7**, 100410 (2022).
- Landau, L. D. Über Die Bewegung der Elektronen in Kristallgitter. *Phys. Z. Sowjetunion* **3**, 644–645 (1933).
- Pekar, S. I. Local quantum states of electrons in an ideal ion crystal. *Zh. Eksp. Teor. Fiz.* **16**, 341–348 (1946).
- Fröhlich, H., Pelzer, H. & Zienau, S. Xx. properties of slow electrons in polar materials. *Philos. Mag.* **41**, 221–242 (1950).
- Fröhlich, H. Electrons in lattice fields. *Adv. Phys.* **3**, 325–361 (1954).
- Holstein, T. Studies of polaron motion: Part ii. the small polaron. *Ann. Phys.* **8**, 343–389 (1959).
- Holstein, T. Studies of polaron motion: Part i. the molecular-crystal model. *Ann. Phys.* **8**, 325–342 (1959).

13. Hock, K., Nickisch, H. & Thomas, H. Jahn-teller effect in itinerant electron-systems-the jahn-teller polaron. *Helvetica Phys. Acta* **56**, 237–243 (1983).
14. Teresa, J. M. D. et al. Evidence for magnetic polarons in the magnetoresistive perovskites. *Nature* **386**, 256–259 (1997).
15. Millis, A. J., Mueller, R. & Shraiman, B. I. Fermi-liquid-to-polaron crossover. ii. double exchange and the physics of colossal magnetoresistance. *Phys. Rev. B* **54**, 5405–5417 (1996).
16. Zhao, G. M., Hunt, M. B., Keller, H. & Müller, K. A. Evidence for polaronic supercarriers in the copper oxide superconductors $\text{La}_{2-x}\text{Sr}_x\text{CuO}_4$. *Nature* **385**, 236–239 (1997).
17. Franchini, C., Reticcioli, M., Setvin, M. & Diebold, U. Polarons in materials. *Nat. Rev. Mater.* **6**, 560–586 (2021).
18. Freysoldt, C., Neugebauer, J. & Van de Walle, C. G. Electrostatic interactions between charged defects in supercells. *Phys. Status Solidi* **248**, 1067–1076 (2011).
19. Lany, S. & Zunger, A. Assessment of correction methods for the band-gap problem and for finite-size effects in supercell defect calculations: Case studies for zno and gaas. *Phys. Rev. B* **78**, 235104 (2008).
20. Sio, W. H., Verdi, C., Poncé, S. & Giustino, F. Polarons from first principles, without supercells. *Phys. Rev. Lett.* **122**, 246403 (2019).
21. Sadigh, B., Erhart, P. & Åberg, D. Variational polaron self-interaction-corrected total-energy functional for charge excitations in insulators. *Phys. Rev. B* **92**, 075202 (2015).
22. Falletta, S. & Pasquarello, A. Many-body self-interaction and polarons. *Phys. Rev. Lett.* **129**, 126401 (2022).
23. Falletta, S. & Pasquarello, A. Hubbard u through polaronic defect states. *npj Comput. Mater.* **8**, 263 (2022).
24. Bondarenko, N., Eriksson, O. & Skorodumova, N. V. Polaron mobility in oxygen-deficient and lithium-doped tungsten trioxide. *Phys. Rev. B* **92**, 165119 (2015).
25. Bousquet, E. et al. First-principles characterization of single-electron polaron in wo_3 . *Phys. Rev. Res.* **2**, 012052 (2020).
26. Salje, E. et al. Crystal structure and paramagnetic behaviour of wo_3 x. *J. Phys. Condens. Matter* **9**, 6563 (1997).
27. Salje, E. K. H. Polarons and bipolarons in tungsten-oxide wo_3 -x. *Eur. J. Solid State Inorg. Chem.* **31**, 805 (1994).
28. Howard, C. J., Luca, V. & Knight, K. S. High-temperature phase transitions in tungsten trioxide - the last word? *J. Phys. Condens. Matter* **14**, 377–387 (2001).
29. Woodward, P., Sleight, A. & Vogt, T. Ferroelectric tungsten trioxide. *J. Solid State Chem.* **131**, 9–17 (1997).
30. Hamdi, H., Salje, E. K., Ghosez, P. & Bousquet, E. First-principles reinvestigation of bulk wo_3 . *Phys. Rev. B* **94**, 245124 (2016).
31. Hassani, H., Partoens, B., Bousquet, E. & Ghosez, P. First-principles study of lattice dynamical properties of the room-temperature p_{21}/n and ground-state p_{21}/c phases of wo_3 . *Phys. Rev. B* **105**, 014107 (2022).
32. Simchi, H., McCandless, B., Meng, T. & Shafarman, W. Structural, optical, and surface properties of wo_3 thin films for solar cells. *J. Alloy. Compd.* **617**, 609–615 (2014).
33. Niklasson, G. A., Berggren, L. & Larsson, A. L. Electrochromic tungsten oxide: the role of defects. *Sol. Energy Mater. Sol. Cells* **84**, 315–328 (2004).
34. Salje, E.K.H. Polaronic states and superconductivity in wo_3 -x. *Condensed Matter* **5**. <https://doi.org/10.3390/condmat5020032> (2020).
35. Shengelaya, A., Mattina, F.L. & Conder, K. Unconventional transport properties of reduced tungsten oxide $\text{wo}_{2.9}$. *Condensed Matter* **5**. <https://doi.org/10.3390/condmat5040063> (2020).
36. Gerosa, M., Di Valentin, C., Onida, G., Bottani, C. E. & Pacchioni, G. Anisotropic effects of oxygen vacancies on electrochromic properties and conductivity of γ -monoclinic wo_3 . *J. Phys. Chem. C* **120**, 11716–11726 (2016).
37. Gerosa, M., Gygi, F., Govoni, M. & Galli, G. The role of defects and excess surface charges at finite temperature for optimizing oxide photoabsorbers. *Nat. Mater.* **17**, 1122 (2018).
38. Gullapalli, S. K., Vemuri, R. S. & Ramana, C. V. Structural transformation induced changes in the optical properties of nano-crystalline tungsten oxide thin films. *Appl. Phys. Lett.* **96**, 171903 (2010).
39. Allen, P. B. & Perebeinos, V. Anti-jahn-teller polaron in lamno_3 . *Phys. Rev. B* **60**, 10747–10753 (1999).
40. Ping, Y. & Galli, G. Optimizing the band edges of tungsten trioxide for water oxidation: a first-principles study. *J. Phys. Chem. C* **118**, 6019 (2014).
41. Wang, F., Valentin, C. D. & Pacchioni, G. Electronic and structural properties of wo_3 : a systematic hybrid dft study. *J. Phys. Chem. C* **115**, 8345–8353 (2011).
42. Wang, W., Janotti, A. & Van de Walle, C. G. Phase transformations upon doping in WO_3 . *J. Chem. Phys.* **146**, 214504 (2017).
43. Kouwenhoven, L. P., Austing, D. G. & Tarucha, S. Few-electron quantum dots. *Rep. Prog. Phys.* **64**, 701 (2001).
44. Walkingshaw, A. D., Spaldin, N. A. & Artacho, E. Density-functional study of charge doping in wo_3 . *Phys. Rev. B* **70**, 165110 (2004).
45. Detraux, F., Ghosez, P. & Gonze, X. Anomalously large born effective charges in cubic wo_3 . *Phys. Rev. B* **56**, 983–985 (1997).
46. Ghosez, P., Michenaud, J. P. & Gonze, X. Dynamical atomic charges: the case of ABO_3 compounds. *Phys. Rev. B* **58**, 6224–6240 (1998).
47. Goldschmidt, V. Die Gesetze der Krystallochemie. *Naturwissenschaften* **14**, 477–485 (1926).
48. Ghosez, P. & Junquera, J. Modeling of ferroelectric oxide perovskites: From first to second principles. *Annu. Rev. Condens. Matter Phys.* **13**, 325–364 (2022).
49. Lenjer, S., Schirmer, O. F., Hesse, H. & Kool, T. W. Conduction states in oxide perovskites: three manifestations of ti^{3+} jahn-teller polarons in barium titanate. *Phys. Rev. B* **66**, 165106 (2002).
50. Shamblyn, J. et al. Experimental evidence for bipolaron condensation as a mechanism for the metal-insulator transition in rare-earth nickelates. *Nat. Commun.* **9**, 86 (2018).
51. Mazzola, F. et al. Unveiling the electronic structure of pseudotetragonal wo_3 thin films. *J. Phys. Chem. Lett.* **14**, 7208–7214 (2023).
52. Haeni, J. H. et al. Room-temperature ferroelectricity in strained srtio_3 . *Nature* **430**, 758–761 (2004).
53. Kim, D. et al. Polar metals by geometric design. *Nature* **533**, 68 (2016).
54. Liao, Z. et al. Metal-insulator-transition engineering by modulation tilt-control in perovskite nickelates for room temperature optical switching. *Proc. Natl Acad. Sci. USA* **115**, 9515–9520 (2018).
55. Varignon, J., Bristowe, N. C. & Ghosez, P. Electric field control of jahn-teller distortions in bulk perovskites. *Phys. Rev. Lett.* **116**, 057602 (2016).
56. Nova, T. F., Disa, A. S., Fechner, M. & Cavalleri, A. Metastable ferroelectricity in optically strained srtio_3 . *Science* **364**, 1075–1079 (2019).
57. Bilc, D. I. et al. Hybrid exchange-correlation functional for accurate prediction of the electronic and structural properties of ferroelectric oxides. *Phys. Rev. B* **77**, 165107 (2008).
58. Causá, M., Dovesi, R., Pisani, C., Colle, R. & Fortunelli, A. Correlation correction to the hartree-fock total energy of solids. *Phys. Rev. B* **36**, 891–897 (1987).
59. Figgen, D., Peterson, K.A., Dolg, M. & Stoll, H. Energy-consistent pseudopotentials and correlation consistent basis sets for the 5d elements hf-pt. *J. Chem. Phys.* **130**. <https://doi.org/10.1063/1.3119665> (2009).
60. Abinit, G. Agate software : an Abinit Graphical Analysis Tool Engine. <https://github.com/abinit/agate>.

Acknowledgements

The author thanks Elaheh Ghorbani for useful discussion. P.G. was supported by F.R.S.-FNRS Belgium through the research project PRO-MOSPAN (grant T.0107.20). All authors acknowledge access to the CECI supercomputer facilities funded by the F.R.S-FNRS (Grant No. 2.5020.1) and to the Tier-1 supercomputer of the Fédération Wallonie-Bruxelles funded by the Walloon Region (Grant No. 1117545).

Author contributions

P.G. conceived the study and supervised the work with B.P. H.H. performed the calculations and analyzed the results. X.H. and H.H. made the search and characterization of alternative compounds. E.B. provided support for the first-principles calculations and B.P. for the development of the quantum dot model. P.G. and H.H. wrote the manuscript. All authors discussed the results during the project and commented the manuscript.

Competing interests

The authors declare no competing interest.

Additional information

Supplementary information The online version contains supplementary material available at <https://doi.org/10.1038/s41467-025-56791-0>.

Correspondence and requests for materials should be addressed to Philippe Ghosez.

Peer review information *Nature Communications* thanks Quintin Meier, and the other, anonymous, reviewer(s) for their contribution to the peer review of this work. A peer review file is available.

Reprints and permissions information is available at <http://www.nature.com/reprints>

Publisher's note Springer Nature remains neutral with regard to jurisdictional claims in published maps and institutional affiliations.

Open Access This article is licensed under a Creative Commons Attribution-NonCommercial-NoDerivatives 4.0 International License, which permits any non-commercial use, sharing, distribution and reproduction in any medium or format, as long as you give appropriate credit to the original author(s) and the source, provide a link to the Creative Commons licence, and indicate if you modified the licensed material. You do not have permission under this licence to share adapted material derived from this article or parts of it. The images or other third party material in this article are included in the article's Creative Commons licence, unless indicated otherwise in a credit line to the material. If material is not included in the article's Creative Commons licence and your intended use is not permitted by statutory regulation or exceeds the permitted use, you will need to obtain permission directly from the copyright holder. To view a copy of this licence, visit <http://creativecommons.org/licenses/by-nc-nd/4.0/>.

© The Author(s) 2025